Crack Fault Diagnosis and Location Method for a Dual-Disk Hollow Shaft Rotor System Based on the Radial Basis Function Network and Pattern Recognition Neural Network

Yuhong Jin[1], Lei Hou[1*] , Zhenyong Lu[2] and Yushu Chen[1]

Abstract

The crack fault is one of the most common faults in the rotor system, and researchers have paid close attention to its fault diagnosis. However, most studies focus on discussing the dynamic response characteristics caused by the crack rather than estimating the crack depth and position based on the obtained vibration signals. In this paper, a novel crack fault diagnosis and location method for a dual-disk hollow shaft rotor system based on the Radial basis function (RBF) network and Pattern recognition neural network (PRNN) is presented. Firstly, a rotor system model with a breathing crack suitable for a short-thick hollow shaft rotor is established based on the finite element method, where the crack's periodic opening and closing pattern and different degrees of crack depth are considered. Then, the dynamic response is obtained by the harmonic balance method. By adjusting the crack parameters, the dynamic characteristics related to the crack depth and position are analyzed through the amplitude-frequency responses and waterfall plots. The analysis results show that the first critical speed, first subcritical speed, first critical speed amplitude, and super-harmonic resonance peak at the first subcritical speed can be utilized for the crack fault diagnosis. Based on this, the RBF network and PRNN are adopted to determine the depth and approximate location of the crack respectively by taking the above dynamic characteristics as input. Test results show that the proposed method has high fault diagnosis accuracy. This research proposes a crack detection method adequate for the hollow shaft rotor system, where the crack depth and position are both unknown.

Keywords Hollow shaft rotor, Breathing crack, Radial basis function network, Pattern recognition neural network, Machine learning

1 Introduction

Rotating machinery is an integral part of modern industry, which has many applications in gas turbines, aero-engine, wind turbines, and other critical machinery equipment. Because the working environment of rotating machinery is harsh, it is easy to generate mechanical failure. The crack fault is one of the most common failure forms in the rotor system [1], which can seriously threaten the reliability of rotating machinery operating. Therefore, timely and accurate fault diagnosis of the crack fault is of great significance in improving the operation reliability of rotating machinery. Since the 1970s, many researchers have studied the crack fault diagnosis of the rotor system in many aspects. Mayes et al. [2] first used a more accurate cosine breathing function to describe the breath behavior of the crack and studied

*Correspondence:
Lei Hou
houlei@hit.edu.cn
[1] School of Astronautics, Harbin Institute of Technology, Harbin 150001, China
[2] Institute of Dynamics and Control Science, Shandong Normal University, Ji'nan 250014, China

Jin *et al. Chinese Journal of Mechanical Engineering*　　(2023) 36:35

Page 2 of 18

the dynamic response of the rotor system containing a breathing crack. Then Al-Shudeifat et al. [3] proposed a new type of breathing function using the Fourier series and compared it with Mayes' results. The comparative results show that this respiration function could more accurately represent the breathing process of crack. Besides, it is found that the super-harmonic resonance can be regarded as the vibration characteristics caused by the crack, and the phenomenon of the natural frequency change with the increase of the crack depth is reported. Darpe et al. [4] analyzed the influence of the interaction of the two cracks on the breathing behavior and the dynamic response of the Jeffcott rotor based on the concepts of fracture mechanics. Significant transformations in the rotor's dynamic response are observed when the angle between the two cracks' directions changes. Xiang et al. [5] considered an asymmetric rotor-bearing system with crack and rub-impact coupling faults under oil-film forces. The effects of crack depth on the onset of instability and nonlinear responses of the rotor-bearing system are studied. Hou et al. [6] found the super-harmonic resonance phenomenon of the cracked rotor due to maneuver load. Lu et al. [7] studied the dynamic response of a hollow shaft dual-rotor system with breathing crack and unbalanced excitation. In the spectrum, it is found that the peak value of the super-harmonic resonance is related to the dimensionless depth of the crack. Fu et al. [8] reported similar results in the dynamic response of a cracked rotor system with uncertain crack parameters. Wang et al. [9] considered the anisotropy in a cracked rotor system and analyzed its parameter instability phenomena. Unlike traditional dynamic analysis methods, Liu et al. [10] developed a novel Nonlinear Output Frequency Response Functions (NOFRFs) based criterion and discussed its application to the cracked rotor system. Through simulations and experiments, they found that some specific index is sensitive to the degree of crack propagation. Most of these studies focus on the dynamic response characteristics of the cracked rotor system or only qualitative analysis of the influence of the crack parameters (such as the depth and location of the crack) [11–13]. However, quantitatively identifying the fault properties based on the dynamic response is necessary for many practical situations. This type of problem is known as fault diagnosis [14].

In recent years, various machine learning methods, such as the artificial neural network (ANN) [15], support vector machine (SVM) [16], and decision-making tree (DT), have been widely applied in various fields. Many researchers also adopt these methods to study the fault diagnosis of the rotor system. Munoz-Abella et al. [17] used the ANN and a large number of simulation data to make the crack fault diagnosis for a simple Jeffcott rotor

and achieved good results. Guo et al. [18] proposed a fault diagnosis method for a Jeffcott rotor with a breathing crack at the early stage of crack propagation based on the empirical mode decomposition (EMD) technology combined with ANN and conducted experimental verification. Vashisht et al. [19] investigated the effect of cracks on a complex rotor system with ball bearing and advanced a crack detection method using the switching control strategy and Short Time Fourier Transform. Yan et al. [20] extracted multi-domain features from the vibration signals by combining multiple signal processing technologies (such as statistical analysis, Variational Mode Decomposition, and Fast Fourier Transform). Then, a novel optimized SVM is adopted to study the fault diagnosis problem of the rotor system. Fault types include a crack in the outer race, an inner race with the spall, and pitting in balls. Comparative test results show that the proposed method is better than the traditional SVM. Bin et al. [21] proposed a new approach for rotating machinery fault diagnosis based on wavelet packet decomposition (WPD)-EMD fault feature extraction and the neural network. Ma et al. [22] presented a diagnosis method for rotor and bearing faults of rotating machinery based on ensemble learning. In this study, the method of weighting and integrating the Convolution Residual Network (CRN), Deep Belief Network (DBN), and Deep AutoEncoder (DAE) obtains a significant effect on the problem of multi-fault classification. Wang et al. [23] determined the crack parameters, including crack location, depth, and angle for a solid shaft by using Kriging Surrogate Model and improved Nondominated Sorting Genetic Algorithm-III (NSGA-III), which has high parameter identification accuracy. Wang et al. [24] used the K-means clustering method to classify crack faults for a planetary gearbox. Li et al. [25] studied multiple crack identification based on the three steps meshing, and experimental verification was also carried out. Most researchers' objects are simple Jeffcott rotors [26–28] or solid shaft rotors [29–31]. Nevertheless, to improve the rotor operating efficiency in practical problems, most large complex rotor systems adopt the hollow shaft. There is relatively little research on crack fault diagnosis of hollow shaft rotor systems.

The crack model of the hollow shaft is more complex than the solid shaft, which leads to a more complex dynamic response, making the crack fault diagnosis more difficult. Besides, many researchers focus on the pattern recognition of the crack fault in the various faults of the rotor system or calculating the crack depth with the fixed crack position. However, in practice, the crack failure may occur at any shaft position. The depth and position of the crack can have a coupling effect on the system's dynamic response, which may confuse the

Jin *et al. Chinese Journal of Mechanical Engineering*   (2023) 36:35

Page 3 of 18

crack diagnosis results. Therefore, identifying the hollow shaft crack's parameters based on the system's dynamic response when the crack depth and position are both uncharted remains challenging.

The motivation of this study is to develop a novel crack fault diagnosis method for a two-disk hollow shaft rotor system. In which both the crack depth and location are uncharted. Considering the crack's periodic opening and closing pattern and different degrees of crack depth, we establish the hollow shaft crack model with the breathing function. The dynamic response of the cracked rotor system is obtained by adopting the Harmonic Balance Method, and some dynamic characteristics related to the crack properties are summarized. Based on this, the Radial basis function (RBF) neural network and pattern recognition network are utilized to solve the crack fault diagnosis problem when the crack's depth and location are both unknown. The effectiveness of the proposed method is verified by simulation.

The paper is organized as follows, in Section 2, the motion equations of the dual-disk hollow shaft rotor system with a breathing crack are constructed by the finite element method. Secondly, in Section 3, the harmonic balance method (HBM) is used to solve the dynamic response of the rotor system, and the effect of crack depth and position is analyzed, respectively. The Runge-Kutta method is used to verify the results of HBM. The crack depth estimation problem is discussed based on the RBF neural network, and the problem of crack location is solved using the pattern recognition network in Section 4. Finally, Section 5 summarizes the primary results of this paper.

2 Dynamic Model of a Dual-disk Hollow Shaft Rotor with a Breathing Crack

2.1 Finite Element Model of the Rotor System

The finite element model of the cracked dual-disk hollow shaft rotor system is shown in Figure 1, divided into 20 elements and 21 nodes. Each end of the rotor (node 1 and node 21) has a bearing and support. There are two disks in this rotor system, which locate at node 5 and node 17, respectively. The shaft of this model is hollow, and its inner radius is denoted as r while its outer radius is R. To fit the actual failure status better,
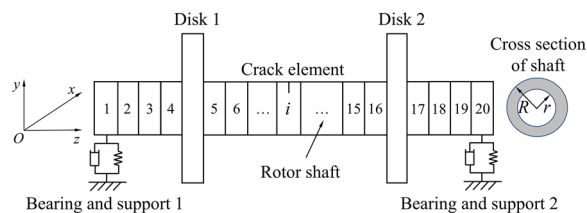
the crack may locate in any element of the shaft. The physical parameters of the model are shown in Table 1.

2.2 Crack Model

The crack in the hollow shaft is more complex than that in the solid shaft. Figure 2 shows different crack conditions under disparate depths, and the dashed area represents the uncracked segment. When the crack is relatively shallow, it is a non-penetrating crack (Figure 2a), and when the crack depth is large, it is a passthrough crack (Figure 1b). A_1 and A_C represent the cross-sectional area of uncracked and cracked segments, respectively. $O\text{-}xy$ is the fixed coordinate system, and $C\text{-}\overline{x}\overline{y}$ is the centroid coordinate system. C is the centroid of section A_1. Ω, h and e represent rotor speed, crack depth, and eccentricity. α and α_1 is the angle between the crack edge and O.

From Figure 2, the moment of inertia of the non-penetrating crack across the x and y-axis can be obtained as follows

Table 1 The physical parameters of the rotor system

Parameters	Value
Shaft length L(m)	0.8562
External radius R(m)	0.0441
Inside radius r(m)	0.0110
Material density ρ(kg/m³)	7800
Young's modulus E(GPa)	2.09
Shear modulus G(GPa)	80.38
Bearing stiffness K(N/m)	5×10^7
Disk 1 diameter d_1(m)	0.1215
Disk 1 mass m_1(kg)	6.5157
Disk 2 diameter d_2(m)	0.1493
Disk 1 mass m_2(kg)	3.9543
Amount of unbalance $m_e d$(kg·m)	5×10^{-7}
Unbalance deflection θ	0
Bearing damping c_{xx}(Ns/m)	1000

Figure 1 Finite element model of a cracked two-disk hollow shaft rotor system
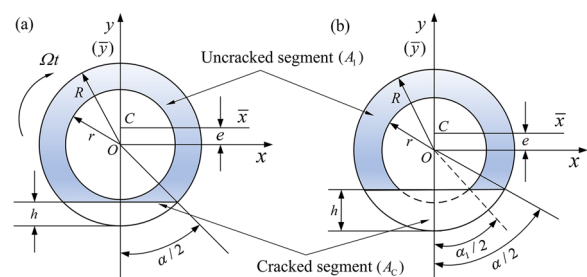

Figure 2 Cross-section diagram of hollow shaft crack: (**a**) Non-penetrating crack, (**b**) Passthrough crack. The dashed area represents the uncracked segment

$$A_1 = R^2(\pi - \cos^{-1}(1 - \lambda) + (1 - \lambda)\gamma) - \pi r^2, \quad (1)$$

$$I_x^C = \frac{\pi R^2}{8} - \frac{R^4}{4}((1 - \lambda)(2\lambda^2 - 4\lambda + 1)\gamma + \sin^{-1}(1 - \lambda)), \quad (2)$$

$$I_y^C = \frac{R^4}{12}((1 - \lambda)(2\lambda^2 - 4\lambda - 3)\gamma + 3\sin^{-1}\gamma), \quad (3)$$

$$e = \frac{2R^3}{3A_1}\gamma^3, \quad (4)$$

where $\lambda = h/R$ represent the dimensionless crack depth and $\gamma = \sqrt{\lambda(2 - \lambda)}$. I_x^C and I_y^C is the moment of inertia of the cracked segment A_C across the x and y-axis.

When the crack is deep, the above equations can be rewritten as

$$A_1 = R^2(\pi - \cos^{-1}(1 - \lambda) + (1 - \lambda)\gamma) - (\pi r^2 - \alpha_1 r^2/2 + (R - h)\sqrt{r^2 - (R - h)^2}), \quad (5)$$

$$I_x^C = R^2(\pi - \cos^{-1}(1 - \lambda)(2\lambda^2 - 4\lambda + 1)\gamma + \sin^{-1}(1 - \lambda)) - \int_{-r}^{h-R} 2x^2\sqrt{r^2 - x^2}\,\mathrm{d}x, \quad (6)$$

$$I_y^C = \frac{R^4}{12}((1 - \lambda)(2\lambda^2 - 4\lambda - 3)\gamma + 3\sin^{-1}\gamma) - \int_{-\sqrt{r^2 - (R-h)^2}}^{0} 2x^2(\sqrt{r^2 - x^2} + h - R)\,\mathrm{d}x, \quad (7)$$

$$e = \frac{2R^3}{3A_1}\gamma^3 - \frac{1}{A_1}\int_{h-R}^{r} 2x^2\sqrt{r^2 - x^2}\,\mathrm{d}x, \quad (8)$$

Supposing $R = 1$ and $r = 0.5$, Figure 3 shows the curve of I_x^C and I_y^C when λ changes from 0 to 1. It can be seen that both I_x^C and I_y^C increase with the increase of λ, but the change trends are different. Furthermore, note that I_x^C and I_y^C are the same value at the dimensionless depth of the crack $\lambda = 1$. This result can be explained by the fact that the cross section of the crack element is a semicircle in this case which has an equal moment of inertia across the x and y-axis. Similar results are also reported in Refs. [3] and [7].

The moment of inertia of the uncracked intact shaft section relative to the x and y axes is denoted as I, then according to the principle of superposition of the moment of inertia, the inertia moment of uncracked segment A_1 can be given as
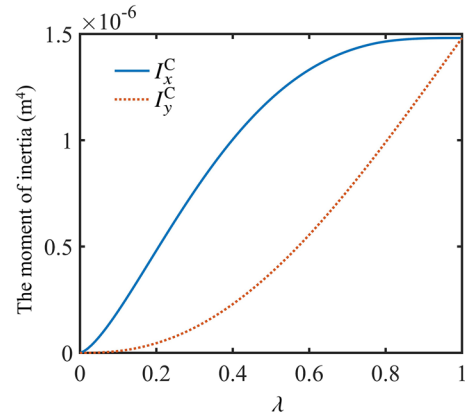
$$I_1 = I - I_x^C, \quad (9)$$

Figure 3 The curve of I_x^C and I_y^C with respect to λ ($R=1$, $r=0.5$)

$$I_2 = I - I_y^C, \quad (10)$$

where $I = \pi(R^4 - r^4)/4$, subsequently, the area moment of inertia of cross-section A_1 relative to the fixed coordinate system O-xy need to convert to the centroid coordinate system C-$\bar{x}\bar{y}$, which can be denoted as $\bar{I}_1$ and $\bar{I}_2$ respectively and obtained by the parallel axis shift theorem as follows

$$\bar{I}_1 = I_1 - A_1 e^2, \quad (11)$$

$$\bar{I}_2 = I_2. \quad (12)$$

During the rotation of the rotor, the crack will periodically open and close due to the influence of the rotor's weight. It is necessary to introduce a breathing function to approximate this process. In this paper, the cosine breathing function proposed by Mayes [1] is adopted, which is given as

$$f(t) = \frac{1}{2}(1 + \cos(\Omega t)), \quad (13)$$

where Ω is the rotational speed. Then the time-varying moment of inertia of the crack element can be calculated as

Jin *et al. Chinese Journal of Mechanical Engineering*   (2023) 36:35

Page 5 of 18

$$I_{\overline{x}}(t) = I - (I - \overline{I}_1)f(t) = I - (I_x^C + A_1 e^2)f(t), \quad (14)$$

$$I_{\overline{y}}(t) = I - (I - \overline{I}_2)f(t) = I - I_y^C f(t). \quad (15)$$

When a crack appears at element j, the time-varying stiffness matrix of the crack element is calculated as follows

$$K_{ce}^{j} = \frac{E}{l^3}\begin{bmatrix} 12I_{\overline{x}}\frac{1}{1+\varphi_1} & 0 & 0 & 6lI_{\overline{x}}\frac{1}{1+\varphi_1} & -12I_{\overline{x}}\frac{1}{1+\varphi_1} & 0 & 0 & 6lI_{\overline{x}}\frac{1}{1+\varphi_1} \\ 0 & 12I_{\overline{y}}\frac{1}{1+\varphi_2} & 6lI_{\overline{y}}\frac{1}{1+\varphi_2} & 0 & 0 & -12I_{\overline{y}}\frac{1}{1+\varphi_2} & -6lI_{\overline{y}}\frac{1}{1+\varphi_2} & 0 \\ 0 & -6lI_{\overline{y}}\frac{1}{1+\varphi_2} & l^2I_{\overline{y}}\frac{4+\varphi_2}{1+\varphi_2} & 0 & 0 & 6lI_{\overline{y}}\frac{1}{1+\varphi_2} & l^2I_{\overline{y}}\frac{2-\varphi_2}{1+\varphi_2} & 0 \\ 6lI_{\overline{x}}\frac{1}{1+\varphi_1} & 0 & 0 & l^2I_{\overline{x}}\frac{4+\varphi_1}{1+\varphi_1} & -6lI_{\overline{x}}\frac{1}{1+\varphi_1} & 0 & 0 & l^2I_{\overline{x}}\frac{2-\varphi_1}{1+\varphi_1} \\ -12I_{\overline{x}}\frac{1}{1+\varphi_1} & 0 & 0 & -6lI_{\overline{x}}\frac{1}{1+\varphi_1} & 12I_{\overline{x}}\frac{1}{1+\varphi_1} & 0 & 0 & -6lI_{\overline{x}}\frac{1}{1+\varphi_1} \\ 0 & -12I_{\overline{y}}\frac{1}{1+\varphi_2} & 6lI_{\overline{y}}\frac{1}{1+\varphi_2} & 0 & 0 & 12I_{\overline{y}}\frac{1}{1+\varphi_2} & 6lI_{\overline{y}}\frac{1}{1+\varphi_2} & 0 \\ 0 & -6lI_{\overline{y}}\frac{1}{1+\varphi_2} & l^2I_{\overline{y}}\frac{2-\varphi_2}{1+\varphi_2} & 0 & 0 & 6lI_{\overline{y}}\frac{1}{1+\varphi_2} & l^2I_{\overline{y}}\frac{4+\varphi_2}{1+\varphi_2} & 0 \\ 6lI_{\overline{y}}\frac{1}{1+\varphi_2} & 0 & 0 & l^2I_{\overline{1}}\frac{2-\varphi_1}{1+\varphi_1} & -6lI_{\overline{y}}\frac{1}{1+\varphi_2} & 0 & 0 & l^2I_{\overline{x}}\frac{4+\varphi_1}{1+\varphi_1} \end{bmatrix}, \quad (16)$$

where $\varphi_1 = \frac{12EI_{\overline{x}}}{\mu A_{ce}Gl^2}$ and $\varphi_2 = \frac{12EI_{\overline{y}}}{\mu A_{ce}Gl^2}$. μ is the Poisson ratio of the material, and l is the element length.

For simplicity, Eq. (16) can also be rewritten in the following form

$$K_{ce}^{j} = K^j - f(t)K_c^j = (K^j - \frac{1}{2}K_c^j) - \frac{1}{2}\cos(\Omega t)K_c^j, \quad (17)$$

where K^j is the stiffness matrix of the intact shaft element, and K_c^j is the reduced stiffness matrix representing the effect of crack.

2.3 The Motion Equation of the Cracked Rotor System

According to the rotor dynamics finite element method, Timoshenko beam theory, and Lagrange equation, the motion equation of a dual-disk hollow shaft rotor with a breathing crack can be given as follow

$$M\ddot{q}(t) + \widehat{C}\dot{q}(t) + (\tilde{K} - \frac{1}{2}K_c\cos\Omega t)q(t) = F_1\cos\Omega t + F_2\sin\Omega t + F_g, \quad (18)$$

where $\tilde{K} = K - 1/2K_c$, $\widehat{C} = C + G$. M, C, G and K represent the global mass matrix, damping matrix, rotation matrix, and stiffness matrix of the entire rotor system, including flexible shaft element, disk, bearing, and support, all of which are $4(N+1) \times 4(N+1)$ matrix, N is the number of elements. K_c is the reduced stiffness matrix of the crack element, which is K_c^j in the element j, and others are 0. $q(t)$ is $4(N+1)$ the displacement vector of nodes. Each node has 2 lateral displacements and 2 bending angles. F_1 and F_2 are the components of the unbalanced excitation in the x and y direction. F_g represents the equivalent gravity force on the node. The specific forms of each matrix and vector in Eq. (18) are shown in the Appendix.

3 Dynamic Response Analysis
3.1 Equation Solving
This paper uses the Harmonic Balance Method (HBM) to solve Eq. (18). HBM supposes that the stable solution of the equation has the finite Fourier series solution

$$q(t) = A_0 + \sum_{j=1}^{p}(A_j\cos(k\Omega t) + B_j\cos(k\Omega t)), \quad (19)$$

where p is the number of harmonics used in HBM, it can be determined according to the accuracy requirement. This paper takes $p = 4$ and inserts Eq. (19) in Eq. (18) yields

$$\begin{bmatrix} \hat{K} & P_{11} & P_{21} & 0 & 0 & 0 & 0 & 0 \\ -P_{11} & P_{31} & 0 & P_{21} & 0 & 0 & 0 & 0 \\ P_{22} & 0 & P_{32} & P_{12} & P_{22} & 0 & 0 & 0 \\ 0 & P_{22} & -P_{12} & P_{32} & 0 & P_{22} & 0 & 0 \\ 0 & 0 & P_{23} & 0 & P_{33} & P_{13} & P_{23} & 0 \\ 0 & 0 & 0 & P_{23} & -P_{13} & P_{33} & 0 & P_{23} \\ 0 & 0 & 0 & 0 & P_{24} & 0 & P_{34} & P_{14} \\ 0 & 0 & 0 & 0 & 0 & P_{24} & -P_{14} & P_{34} \end{bmatrix}\begin{bmatrix} A_1 \\ B_1 \\ A_2 \\ B_2 \\ A_3 \\ B_3 \\ A_4 \\ B_4 \end{bmatrix} = \begin{bmatrix} \tilde{F}_1 \\ F_2 \\ 0 \\ 0 \\ 0 \\ 0 \\ 0 \\ 0 \end{bmatrix}, \quad (20)$$

Jin *et al. Chinese Journal of Mechanical Engineering*   (2023) 36:35

Page 6 of 18

where $\widehat{\boldsymbol{K}} = \tilde{\boldsymbol{K}} - \Omega^2 \boldsymbol{M} - 1/8\boldsymbol{K}_c\tilde{\boldsymbol{K}}^{-1}\boldsymbol{K}_c$, $\boldsymbol{P}_{1i} = i\Omega\widehat{\boldsymbol{C}}$, $\boldsymbol{P}_{2i} = 1/4\boldsymbol{K}_c$, $\boldsymbol{P}_{3i} = \tilde{\boldsymbol{K}} - (i\Omega)^2\boldsymbol{M}$, $\tilde{\boldsymbol{F}}_1 = \boldsymbol{F}_1 - 1/2\boldsymbol{K}_c\tilde{\boldsymbol{K}}^{-1}\boldsymbol{F}_g$, $i = 1, 2, 3, 4$. After solving the linear equations of Eq. (20) to obtain the coefficients of each harmonic component, the direct component $\boldsymbol{A}_0$ can be calculated as follow

$$\boldsymbol{A}_0 = \tilde{\boldsymbol{K}}^{-1}(\boldsymbol{F}_g - \frac{1}{4}\boldsymbol{K}_c\boldsymbol{A}_1), \tag{21}$$

The dynamic response of the cracked rotor can be obtained by Eqs. (19)–(21). When there is no crack fault in the dual-disk hollow shaft rotor system, the first 4 order critical speeds are $\omega_1 = 825.1$ rad/s, $\omega_2 = 1359.2$ rad/s, $\omega_3 = 1415.6$ rad/s, and $\omega_4 = 2183.0$ rad/s according to the physical parameters in Table 1.

3.2 Effects of Dimensionless Crack Depth

The position of the crack c_p is fixed at element 10, and Figure 4 shows the 3D waterfall diagram of rotor speed-dimensionless crack depth-amplitude at node 10 under the low speed (near the first critical speed ω_1). Node amplitude is defined as

$$a_i = \sqrt{u_i^2 + v_i^2}, \tag{22}$$

where a_i is the amplitude of node i, u_i is the horizontal displacement of node i, and v_i is the vertical displacement of node i. Analysis from Figure 4 shows that the rotor system has obvious resonance peaks near the first critical speed. Besides, compared to the rotor system without the crack, the cracked rotor system appears super-harmonic resonances (or called subcritical resonances) near 1/2, 1/3, or even 1/4 first-order critical speed due to the crack's occurrence. When the crack depth is relatively shallow, the rotor system first appears to have apparent super-harmonic resonance peaks at $1/2\,\omega_1$ and $1/3\,\omega_1$. As the crack depth gradually increases, a super-harmonic
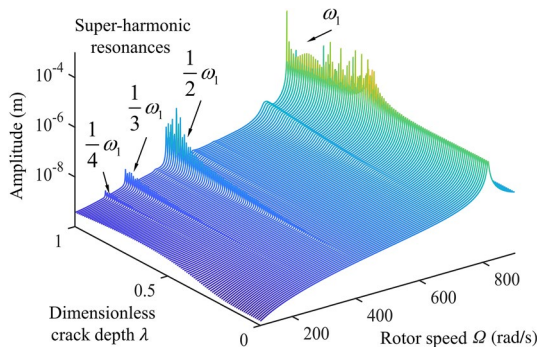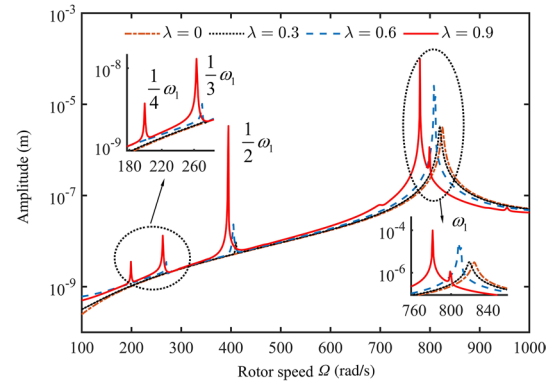

Figure 5 Amplitude-frequency response curves for different crack depths at node 10 ($c_p = 10$)

resonance peak appears at $1/4\,\omega_1$. But compared to the peaks at $1/2\,\omega_1$ and $1/3\,\omega_1$, the resonance peak at $1/4\,\omega_1$ is weak. Furthermore, another pattern we can observe in Figure 4 is that with the dimensionless crack depth improves, the super-harmonic resonance peaks near $1/n\,\omega_1$ ($n=2, 3, 4$) tend to be obvious, indicating that the peak value of the super-harmonic resonances is closely related to λ. Moreover, Figure 5 shows the amplitude-frequency response curves at node 11 with $\lambda = 0, 0.3, 0.6, 0.9$, and $c_p = 10$. It can be observed that the crack slightly reduces the first-order critical speed of the rotor system, and with the increase of crack depth, the super-harmonic resonance peaks become more evident.

Overall, the crack can lead to super-harmonic resonance phenomena near $1/n\,\omega_1$ ($n=2, 3, 4$). The first critical speed and the peak value of super-harmonic resonance (or called subcritical speed amplitude) are closely related to the dimensionless crack depth. These dynamic characteristics can be used to estimate crack depth.
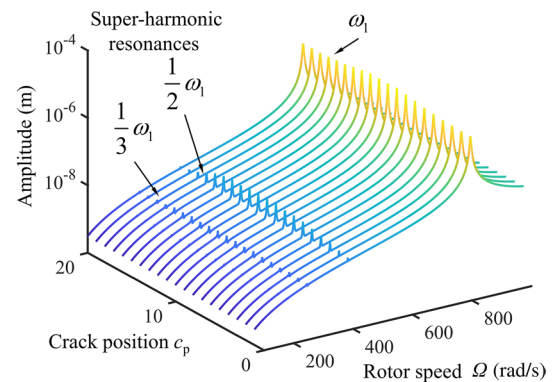

Figure 4 3D waterfall diagram of rotor speed-dimensionless crack depth-amplitude at node 10 ($c_p = 10$)

Figure 6 3D waterfall diagram of rotor speed-crack position-amplitude at node 10 ($\lambda = 0.5$)

Jin *et al. Chinese Journal of Mechanical Engineering* (2023) 36:35

Page 7 of 18

3.3 Influence of Crack Position

The dimensionless crack depth λ is fixed at 0.5, and Figure 6 shows the 3D waterfall diagram of rotor speed-crack position-amplitude at node 10 under the low speed (near the first critical speed ω_1) at the different crack positions. From Figure 6, it can be seen that when the crack is located at both ends of the rotor system, the effect on the dynamic response of the rotor system is weak, and the peak value of super-harmonic resonance in amplitude-frequency response is unobvious. Conversely, as the crack gradually approaches the middle of the rotor system, the subcritical speed amplitude increases. When the crack is located in the middle of the rotor system, the super-harmonic resonance is most apparent. The crack has the most significant impact on the system's dynamic response. These analysis results indicate that the subcritical speed amplitude near $1/n$ ($n = 2, 3, 4$) first critical speed of the rotor system is related to the crack position.

The crack position also has a specific influence on the critical speed of the rotor system. Figure 7 shows the amplitude-f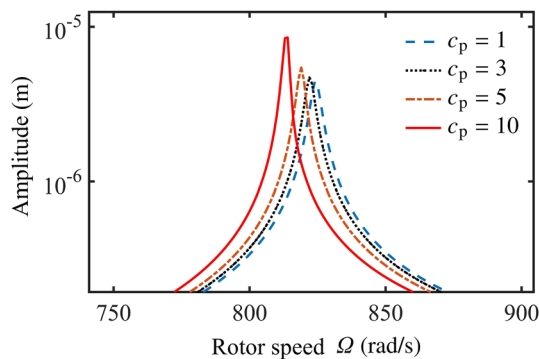requency response curves at node 10 near the main resonance area when the crack is located at elements 1, 3, 5, and 10, where the corresponding first critical speed is 824.3 rad/s, 822.1 rad/s, 819 rad/s, and 814.6 rad/s separately. As the position of the crack moves to the middle of the rotor system, the rotor system's critical speed decreases. When the crack is located in the middle of the rotor system, the critical speed of the rotor system is the lowest.

In short, the crack position affects the dynamic response of the rotor system. As the crack approaches the middle of the rotor system, the shift in the critical and subcritical speeds increases. Besides, the more obvious main resonance peak and subcritical speed amplitude in the amplitude-frequency response can also be observed. Similar conclusions have been confirmed in Ref. [3]. These dynamic characteristics can be tracked for the rotor system to identify the crack position.

3.4 Numerical Verification

In order to verify the accuracy of the HBM adopted in this paper, Section 3.4 uses the Runge-Kutta method (R-K) to solve Eq. (18) and compares its results with the HBM's solutions. Figure 8 shows the time history, whirl orbits, and frequency spectrum solved by HBM and R-K for $\lambda = 0.3$, $c_p = 10$, and $\Omega = 500$ rad/s. It can be seen that the calculation results match well. The rotor's orbit is an ellipse, and there are no multiple frequency components in the frequency spectrum, which indicates that there is no super-harmonic resonance phenomenon in the rotor system.

Moreover, Figure 9 compares the time history, whirl orbits, and frequency spectrum solved by HBM and R-K for $\lambda=0.3$, $c_p = 10$, and $\Omega = 410$ rad/s $\approx 1/2\omega_1$. The super-harmonic resonance occurs at this operating speed. It can be seen from Figure 9 that in the case of super-harmonic resonance, the calculation results of the HBM and R-K are still close, further demonstrating
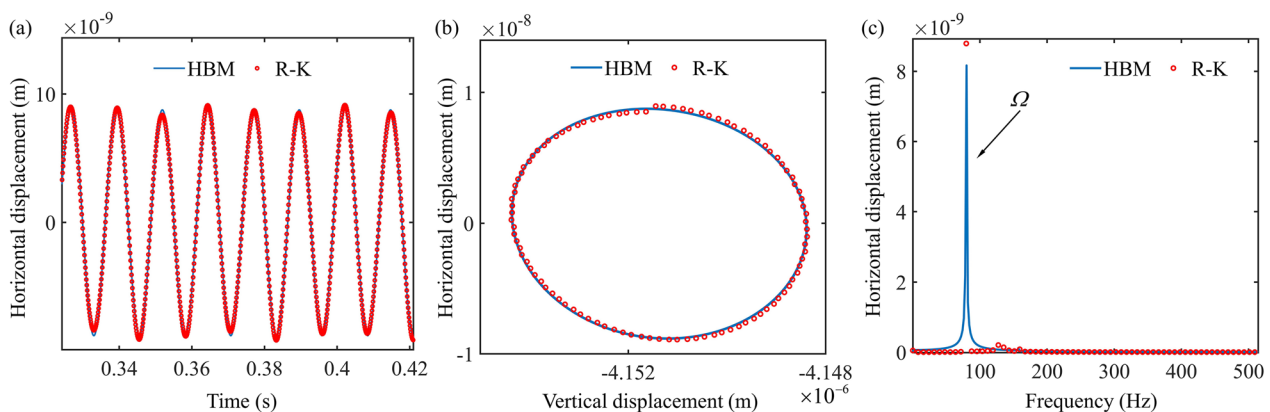

Figure 7 Amplitude-frequency response curves for different crack positions at node 10 ($\lambda = 0.5$)

Figure 8 Comparison of time history, whirling orbits, and frequency spectrum for $\lambda = 0.3$, $c_p = 10$, and $\Omega = 500$ rad/s at node 10: (**a**) Time history, (**b**) Whirl orbits, (**c**) Frequency spectrum

Jin *et al. Chinese Journal of Mechanical Engineering* (2023) 36:35
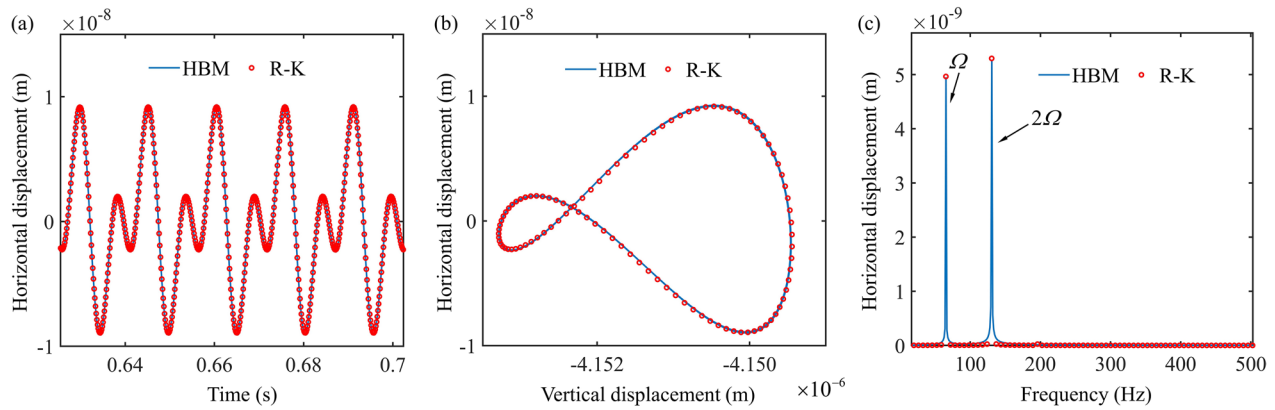
Page 8 of 18

Figure 9 Comparison of time history, whirling orbits, and frequency spectrum for $\lambda = 0.3$, $c_p = 10$, and $\Omega = 410$ rad/s $\approx 1/2\omega_1$ at node 10: (**a**) Time history, (**b**) Whirl orbits, (**c**) Frequency spectrum
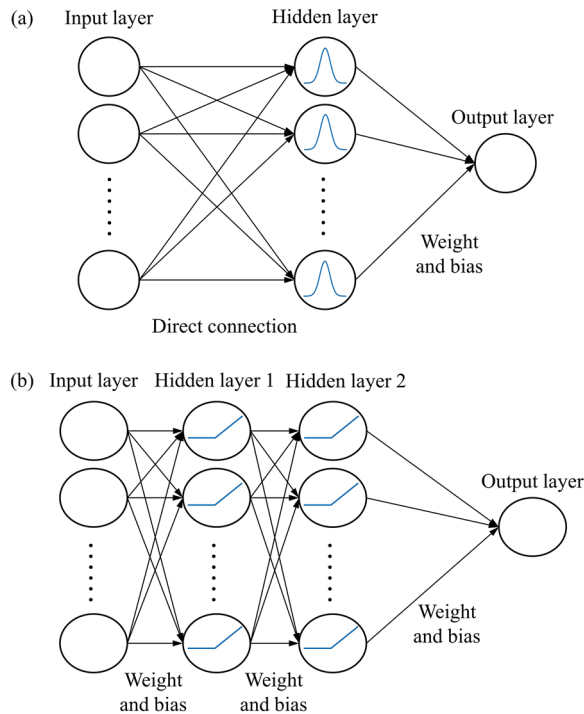

Figure 10 Structure of RBF and BP neural network: (**a**) RBF neural network, (**b**) BP neural network

Figure 11 The image of the Gaussian function (the input dimension is 2)

the accuracy of the HBM. The whirling orbits of the rotor system present shape with two closed loops. At the same time, the 2× frequency component can be observed in the frequency spectrum.

4 The Crack Fault Diagnosis Method for the Hollow Shaft Rotor System based on the Neural Network

4.1 Radial Basis Function Neural Network

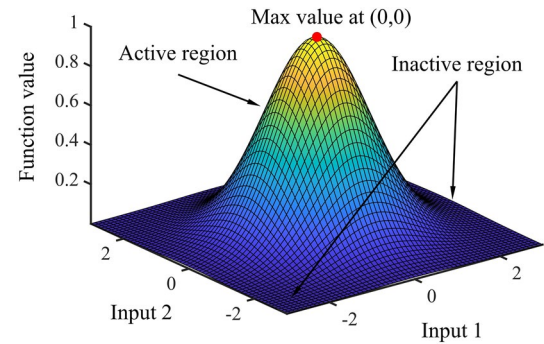The Radial Basis Function (RBF) neural network is a feedforward, fully connected neural network. Compared with the traditional Background Propagation (BP) neural network, the RBF network generally contains only one hidden layer. The radial basis function is utilized as the activation function in the hidden layer. Note that the RBF neural network adopts a direct connection between the input layer and hidden layer instead of a weight connection, as shown in Figure 10.

The output of the RBF network can be defined as

$$y_i = \sum_{j=1}^{q} W_{ij}\rho(\boldsymbol{x}, \boldsymbol{c_j}) + b_i, \tag{23}$$

where $\boldsymbol{x}$ is the input vector of the RBF network, and $\rho(\boldsymbol{x}, \boldsymbol{c_j})$ is the activation function of the jth hidden layer neuron. $\boldsymbol{c_j}$ is the center of radial basis function in the jth hidden layer neuron. W_{ij} represents the weight between the jth hidden layer neuron and the ith output layer neuron, and b_i is the bias parameter of the ith output layer neuron. q is the number of hidden layer neurons, and y_i is the output value of the ith output layer neuron. There are various forms of the radial basis functions in the RBF

network, and the most commonly used is the Gaussian function, which is given as

$$\rho(\boldsymbol{x}, \boldsymbol{c}) = \exp(-\frac{\|\boldsymbol{x} - \boldsymbol{c}\|_2^2}{2\sigma^2}), \tag{24}$$

where $\|\boldsymbol{x} - \boldsymbol{c}\|_2$ represents the Euclidean norm, which is used to characterize the distance between the input vector and the center of the radial basis function. σ is the spread constant of the RBF, affecting the size of the radial basis function's activation region. When the input dimension is 2, take the spread constant as 1, and the center is (0,0), then the Gaussian function is shown in Figure 11. It can be seen from Figure 11 that the Gaussian function has a relatively sensitive response near the center, while the function value in most areas far away from the center is almost 0 (which means inactive). The property of local activation allows the RBF network to set up more neurons without overfitting.

4.2 Calculate the Dimensionless Crack Depth with the RBF Neural Network

The dimensionless depth and position of the crack are assigned by random numbers. Then the dynamic response of the cracked rotor system can be obtained by adopting the methodology in Section 3. The dynamic characteristics related to the crack parameters (including the first critical speed, first subcritical speed, first critical speed amplitude, and the super-harmonic resonance peak at the first subcritical speed) are taken as the input of the RBF network. The output of the RBF network is the predicted dimensionless crack depth. Take 70% data as the training set, 15% as the validation set, and 15% as the test set. Some provided data are shown in Tables 2 and 3. Note that the rotor's amplitude is generally minimal (on the order of 10^{-6}), which is detrimental to the training and computing of the network. Therefore, this paper takes the logarithm (denoted as log in Tables 2 and 3) of the first critical speed amplitude and the first subcritical speed amplitude.

Table 2 Part of the data used to train the RBF network

λ	c_p	First critical speed (rad/s)	First critical speed amplitude (log)	First subcritical speed (rad/s)	First subcritical speed amplitude (log)
0.4050	4	822	−5.4783	411	−8.0111
0.3086	10	820	−5.4808	410	−8.0141
0.3149	19	824	−5.5058	412	−8.1428
0.3384	20	825	−5.5032	412	−8.0971
0.3507	13	820	−5.5021	410	−7.9737
0.3919	11	817	−5.4271	409	−7.9061
0.4295	1	824	−5.4968	412	−7.9544
0.4328	3	823	−5.4879	411	−7.9721
0.4749	6	818	−5.3933	409	−7.8852
0.4947	17	821	−5.4587	411	−7.9143

Table 3 Part of the data used to validate and test the RBF network

Λ	c_p	First critical speed (rad/s)	First critical speed amplitude (log)	First subcritical speed (rad/s)	First subcritical speed amplitude (log)
0.5740	4	820	−5.4097	410	−7.8359
0.3204	6	821	−5.4837	411	−8.0734
0.3889	15	820	−5.4652	410	−7.9463
0.5191	10	813	−5.0707	406	−7.7704
0.32279	5	822	−5.4847	411	−8.0861
0.3319	8	820	−5.4774	410	−8.0090
0.3450	14	820	−5.4742	410	−7.9882
0.3488	3	823	−5.4874	412	−8.0571
0.3512	5	822	−5.4925	411	−8.0536
0.3536	9	819	−5.4659	409	−7.9957

Table 4 Training parameters of the RBF network

Loss function	Max epochs	Spread constant	Steps of validation failure	Clustering algorithm	Training algorithm
MSE	100	0.8	6	k-means	OLS

The mean square error (MSE) function is used as the loss function to train the RBF neural network, which is described as

$$\text{MSE} = \frac{1}{m}\sum_{k=1}^{m}\sum_{j=1}^{o}(\hat{y}_j^k - y_j^k)^2, \tag{25}$$

where o is the number of output layer neurons, m is the sample size, $\hat{y}_j^k$ is the output of the jth neuron for the kth sample input, and y_j^k represents the actual jth output of the kth sample input. The training parameters are summarized in Table 4. The spread constant of the RBF network is 0.8. The steps of validation failure are 6, which means that the training process is stopped early when the loss function on the validation set is no longer descending for 6 consecutive epochs. The selection algorithm for the radial basis function's center adopts the k-means clustering algorithm. The training algorithm is the Ordinary Least Square (OLS) with a closed-form solution, which is very efficient. The RBF network gradually reduces the loss function by adding the number of hidden layer
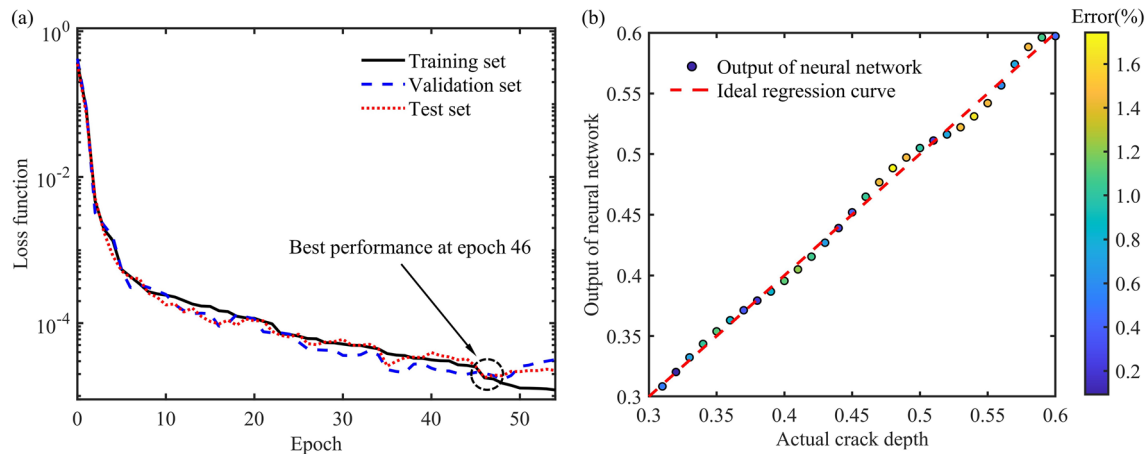

Figure 12 Training and test results of the RBF network when the crack is located in the middle of the rotor system: (**a**) Loss function curve, (**b**) Regression output
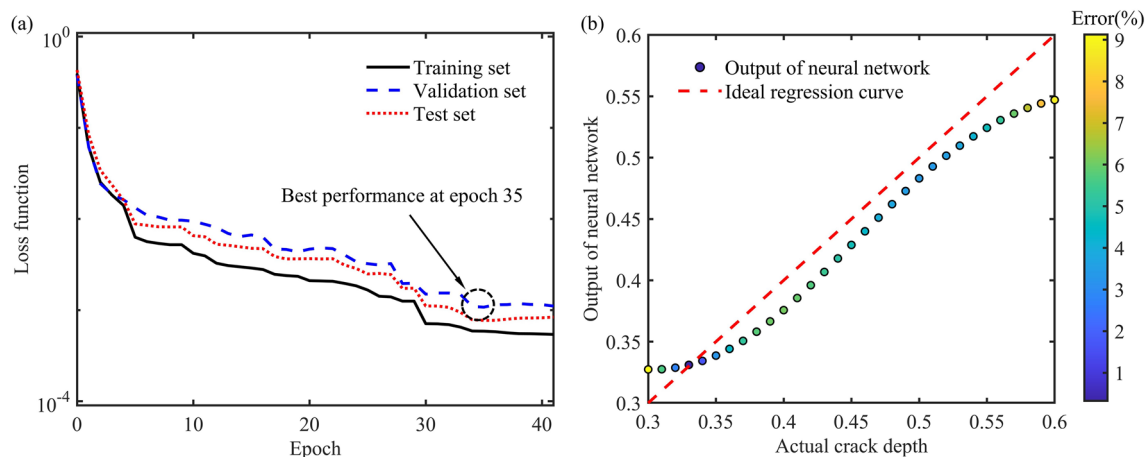

Figure 13 Training and test results of the RBF network when the crack is located at the end of the rotor system: (**a**) Loss function curve, (**b**) Regression output
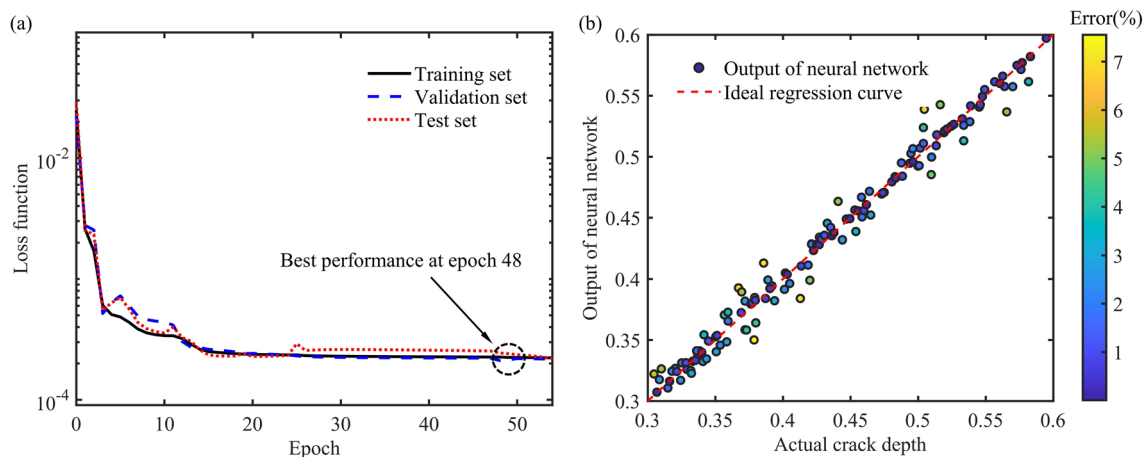
Figure 14 Training and test results of the RBF network when the crack position is uncertain: (**a**) Loss function curve, (**b**) Regression output

neurons one by one from 0, so there is no need to set the initial number of hidden layer neurons in advance.

Figures 12, 13, 14 illustrate the training and test results of the RBF network under three conditions: (1) the crack is in the middle of the rotor system ($c_p = 10$); (2) the crack is at the end of the rotor system ($c_p = 1$); (3) the crack position is uncertain.

When the crack is located in the middle of the rotor system, it can be seen from Figure 12a that the loss function of the training set, validation set, and test set all show an oscillating downward trend with the increase in the number of training epochs. The loss function value of the validation set is minimized at the 48th step, and the training process terminates in advance at the 54th epoch. At the end of the training, the loss function value of the training set is 1.21×10^{-5}, the validation set is 3.16×10^{-5}, and the test set is 2.24×10^{-5}. All three values are reduced to the order of 10^{-5} and with little difference, indicating that the RBF network has great generalization ability. Besides, it can be seen from Figure 12b that the scatter points of the neural network output almost all fall on the ideal regression curve. The correlation coefficient (denoted as CC) between the output results of the neural network and the ground truth is 0.9985, and the maximum percentage error is 1.8%. These results indicate that the RBF neural network can accurately estimate the crack depth based on the provided dynamic characteristics. According to the analysis results in Section 3, when the crack (with the same dimensionless depth) is located in the middle of the rotor system, the impact on the system's dynamic response is the greatest. The shift in the critical and subcritical speeds is the most obvious, and the subcritical amplitude in the amplitude-frequency response is the most significant. More specifically, the dynamic characteristics related to the crack are the most obvious,

which is a benefit for the fault diagnosis. Hence, when the crack is located in the middle of the rotor system, the RBF network can get a satisfactory result for calculating the crack depth.

When the crack is located at the end of the rotor system, related results are summarized in Figure 13. It can be seen from the data in Figure 13a that the loss function of the training set, test set, and validation set decreases with the increase of training epochs. The RBF neural network achieves the best performance at the 35th epoch, and the training process terminates prematurely at the 41st epoch. At the end of the training, the loss function value of the training set is 5.42×10^{-4}, the verification set is 1.08×10^{-3}, and the test set is 8.40×10^{-4}. Compared with the results in Figure 12a, the loss function value is larger. In addition, as shown in Figure 13b, when the crack is relatively shallow, many output results of the RBF network deviate from the ideal regression curve compared with Figure 12b. The maximum percentage error is 9.3%, indicating that the network's performance declined slightly. These results are likely related to the bearing and support with great rigidity. As mentioned in Section 3, when the crack is located at the end of the rotor system, its effects on the system's dynamic response are relatively small. Therefore, the dynamic characteristics related to the crack parameters may be insignificant, which results in a decrease in the RBF network's fault diagnosis performance. However, on the other hand, cracks in this position are also less likely to cause serious consequences.

Note that Figures 12 and 13 are the results of estimating the dimensionless crack depth when the crack position is fixed. However, in actual engineering problems, the crack may appear in various positions in the rotor system. Figure 14 provides the training and test results of the RBF network when c_p is uncertain. From
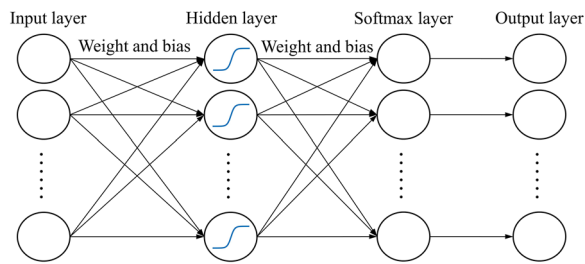
Figure 15 The structure of the pattern recognition network

Figure 14, it can be observed that during the training process, the loss function value of the training set oscillates and decays in a small range with the number of iteration epochs increasing. The loss function value of the validation set is minimized at the 48th epoch, and the training process terminates prematurely at the 56th epoch. When the training is terminated, the loss function value of the training set is 2.19×10^{-4}, and the test set is 2.23×10^{-4}. Both are relatively small and not significantly different, indicating no severe overfitting. The performance of the RBF network can be seen more intuitively from the regression output results in Figure 14(b). Most regression output results are around the ideal regression curve without significant deviation. The correlation coefficient CC between the RBF network's outputs and the sample results is 0.9916, indicating an excellent linear correlation. Besides, the maximum percentage error is 7.6%, which demonstrates an accurate estimation result. The above analysis results show that even in the case of uncertain crack locations, the RBF network can use dynamic characteristics to calculate the crack depth and achieve sufficient precision.

4.3 Pattern Recognition Neural Network

The pattern recognition neural network (PRNN) is a kind of neural network adopted to solve classification problems. Its architecture is set out in Figure 15.

The input first undergoes an affine transformation to the hidden layer. And then, to achieve the nonlinear mapping, an activation function should be introduced. The most common activation function used in the PRNN's hidden layer is the Tan-sigmoid function, which is described as

$$f(x) = \frac{e^x - e^{-x}}{e^x + e^{-x}}. \tag{26}$$

Then, another affine transformation is defined in the Softmax layer, which is utilized to adjust the dimension of the hidden layer's output. Besides, to obtain the

discrete probability density, there is a so-called Softmax function in the Softmax layer, which is given as

$$y_i = \text{softmax}(x_i) = \frac{\exp(x_i)}{\sum\limits_{i=1}^{n} \exp(x_i)}, \tag{27}$$

where $\boldsymbol{x} = [x_1, x_2, ..., x_n]^{\mathrm{T}}$ is the input vector. Eq. (27) has the following properties: (1) each element in the obtained output vector $\boldsymbol{y} = [y_1, y_2, ..., y_n]^{\mathrm{T}}$ is non-negative; (2) the sum of all elements in $\boldsymbol{y}$ is 1. Therefore, $\boldsymbol{y}$ can represent the discrete probability density, and the position of the maximum value in y can be utilized as the classification result. For instance, if the PRNN's output result is $[0.1, 0.6, 0.3]^{\mathrm{T}}$, the corresponding input should be classified into the second category.

4.4 Identification of the Crack Position with PRNN

Similar to Section 4.2, the dynamic characteristics related to the crack position (the first critical speed, first critical speed amplitude, first subcritical speed, and first subcritical speed amplitude) are taken as the PRNN's input. The output of the PRNN is the discrete probability density of the crack position (20 elements). The training, validation, and test sets are the same as in Section 4.2.

Calculating the dimensionless crack depth can be considered a regression problem, so MSE (shown in Eq. (25)) is adopted as the loss function to train the RBF network. Unlike this, identifying the crack position is a pattern recognition problem (known as a classification problem), so an additional loss function should be introduced to train the PRNN. Cross entropy is a popular candidate, which meaning is to characterize the similarity of the probability distribution of two events. Its formula can be calculated as

$$\text{Crossentropy}(P, Q) = -\sum_{i=1}^{n} P(x_i)\log(Q(x_i)), \tag{28}$$

where $P(x_i)$ is the actual probability distribution of event x_i, and $Q(x_i)$ is the discrete probability density of event x_i obtained by the PRNN. In particular, in the classification problem, $P(x_i)$ is a sparse vector, where the position of the actual category is 1 and all the other elements are 0 (known as the one-hot encoding).

Table 5 Training parameters of the PRNN

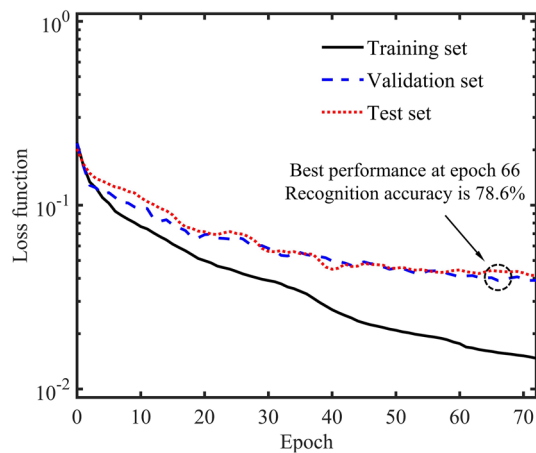| Loss function	Number of hidden neurons	Max epochs	Steps of validation failure	Initial learning rate	Training algorithm
Cross entropy	15	100	6	0.001	L-M

Figure 16 The loss function curve of the PRNN in the training process

Some other training parameters are summarized in Table 5. The number of hidden neurons is 15. The steps of validation failure are 6, which means that the training process is stopped early when the loss function of the validation set is no longer descending for 6 consecutive times. The initial learning rate is 0.001, and the training algorithm adopts Levenberg-Marquardt backpropagation (L-M), which takes up more storage space but is faster.

Based on these parameters, the loss function curves of the training and test sets are shown in Figure 16. It can be observed that the loss function of the training set oscillates and decreases with the training epochs increasing. Similar patterns are also presented in the validation and test sets. The loss function value of the validation set is minimized at the 66th epoch, and the training process terminates in advance at the 72nd epoch. When the training process is finished, the loss function values on the training, validation, and test sets are 0.0147, 0.0390, and 0.0415, respectively. The loss function values on the training and test sets are close, indicating that the trained PRNN has good generalization ability. The recognition accuracy in the test and validation sets is 78.6%, which achieves the basic requirements for identifying the crack position.

Furthermore, in pattern recognition problems, in addition to the obtained recognition accuracy, the causes of classification errors also need attention. Figure 17 shows
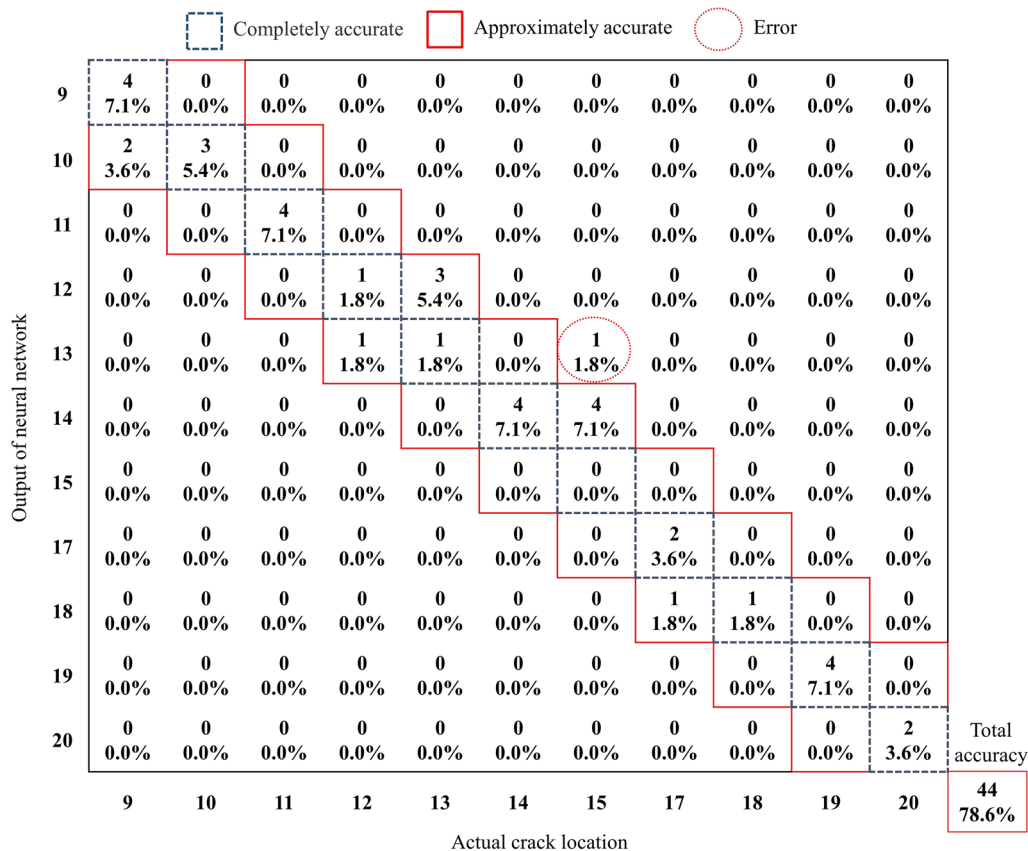

Figure 17 The confusion matrix between the PRNN's output results and the actual crack position

the confusion matrix between the PRNN's output results and the actual crack positions. Note that only the part containing the misclassified results is provided for simplicity. As can be seen from Figure 17, most of the non-zero elements of the confusion matrix are concentrated on the diagonal (dashed area), which means that the PRNN accurately identifies the crack position in most cases. Moreover, careful analysis of the misclassified elements in the confusion matrix can be found that most of the incorrectly classified PRNN output values are only one unit away from the actual crack position. For example, as shown in row 14 in Figure 17, there are 4 cracks in element 15. However, they are misclassified in element 14 by the trained PRNN. A possible explanation for this might be that the dynamic characteristics of the PRNN's input are related to both the crack depth and position. This coupling effect confuses the results of crack location. Nevertheless, when the shaft is divided into 20 elements, the element length is very small. Therefore, the deviation of 1 element length in determining the crack position may not cause a severe problem. Based on this consideration, the condition for evaluating the recognition accuracy can be extended to the recognition deviation within 1 element length. For instance, if the predicted crack position of the PRNN is 12 or 14, while the actual crack position is 13, it can also be considered that the PRNN's output is approximately accurate. Accordingly, it can be seen from Figure 17 that almost all the elements in the confusion matrix fall in the approximately accurate area (red line region). Only 1 instance of the 56 samples has a recognition deviation of 2 element lengths (the actual crack location is 15, but the PRNN's output is 13). The approximate recognition accuracy of the crack position is 98.2%, which is a brilliant result. The above analysis shows that PRNN can utilize the dynamic characteristics of the cracked rotor system to determine the crack position and achieve a high approximate identification accuracy.

4.5 Comparison with Other Crack Diagnosis Methods

To further illustrate the effectiveness and superiority of the proposed method, several alternative machine

Table 6 Dimensionless crack depth calculating results obtained by different crack diagnosis methods on the test set

Method	MSE on the test set	Maximum percentage error(%)
MLR	9.75×10^{-4}	16.2
SVR	5.56×10^{-4}	13.2
KSVR	3.28×10^{-4}	10.6
RBF (proposed)	2.23×10^{-4}	7.6

Table 7 Crack position identification results obtained by different crack diagnosis methods on the test set

Method	Accuracy(%)
KNN	44.6
SVM	48.2
KSVM	50.0
PRNN (proposed)	78.6

learning-based methods for crack diagnosis are implemented. As mentioned previously, calculating the dimensionless crack depth can be considered a regression problem. Correspondingly, the following methods are utilized to conduct a comparison test: (1) multiple linear regression (denoted as MLR); (2) support vector regression (denoted as SVR); (3) support vector regression with kernel function (denoted as KSVR). Similarly, identification of crack position is a pattern recognition problem, so the following methods are considered: (1) K-nearest neighbor algorithm (denoted as KNN); (2) support vector machine (denoted as SVM); (3) support vector machine with kernel function (denoted as KSVM).

The crack diagnosis results obtained from different methods on the test set are summarized in Tables 6 and 7. Note that for a fair comparison, all mentioned methods share the same training set, and their hyperparameters are optimized based on the validation set. As can be seen from Table 6, MLR gives the worst results for calculating the dimensionless crack depth under the same conditions, which indicates that the relationship between the dimensionless crack depth and the system's dynamic response characteristics cannot be represented by a simple linear equation. More accurate diagnosis results can be obtained by adopting the support vector regression, in which introducing the kernel function can improve the nonlinear mapping capability of SVR, thus enhancing its diagnosis performance. However, the maximum percentage error of SVR and KSVR on the test set is still greater than 10%, which is higher than the proposed method (RBF).

In a similar manner, it can be seen from the data in Table 7 that the distance-based KNN method has a poor property for crack position identification. Only 44.6% accuracy is achieved. In contrast, SVM demonstrated better diagnosis performance on the test set, and the nonlinear kernel function is beneficial. However, the crack position identification accuracy of the KNN, SVM and KSVM is not higher than 50%, while our proposed method (PRNN) reaches 78.6%.

Overall, compared with other crack diagnosis methods, RBF neural network and PRNN model realize the best diagnosis results in dimensionless crack depth calculating

and crack position identification, respectively. The above comparison further illustrates the effectiveness of our proposed method.

5 Conclusions

In this paper, a dual-disk hollow shaft rotor system model with a breathing crack is established, where two different crack forms (non-penetrating and passthrough crack) are considered. Then, the dynamic response of the cracked rotor system is obtained through the HBM, and the dynamic characteristics related to the crack parameters are summarized by analyzing the amplitude-frequency curve and waterfall plot. Based on this, a novel crack fault diagnosis and location method based on the RBF network and PRNN is proposed. The main conclusions are as follows.

(1) Due to introducing the time-varying stiffness, the crack can cause the super-harmonic resonance phenomenon in the rotor system near $1/n$ ($n=2,3,4$) first critical speed. Besides, the crack can reduce the stiffness of the system, resulting in a decrease in the system's critical speed.
(2) The analysis results of the cracked rotor system's amplitude-frequency curves and waterfall plots with different crack parameters reveal the dynamic characteristics related to the crack depth and position. The first critical speed, first subcritical speed, first critical speed amplitude, and first subcritical

(4) Several alternative machine learning-based crack fault diagnosis methods are considered in the comparison experiment. The results show that the approach developed in this paper achieves the optimal fault diagnosis performance, further demonstrating its effectiveness.

In future work, further research should focus on the following aspects. Firstly, the proposed method relies on the analyzed dynamic characteristics, such as the super-harmonic resonance peak, which maintain its theoretical basis and interpretability. However, at the same time, noise and nonlinearities can introduce disturbances to these dynamic characteristics and thus confuse the diagnosis results. The robustness of the proposed method regarding interference needs to be further improved. Combining the signal processing methods with the proposed approach may be a good solution. Secondly, limited by the finite element model, the proposed method can only give the approximate crack position. Modeling technology that can accurately describe the crack's location should be further studied. Finally, experimental verification is necessary. In this paper, the validation of the proposed method is based on simulation data. In the future, we will establish the cracked rotor system experiment bench and validate our proposed method with experimental data.

Appendix
Timoshenko beam finite element matrices in Eq. (18)

$$\boldsymbol{K}_s^c = \frac{EI}{(1+\varphi_s^2)l^3}\begin{bmatrix} K_{s1}^c & & & & & & & \text{sym.} \\ 0 & K_{s1}^c \\ 0 & -K_{s2}^c & K_{s3}^c \\ -K_{s2}^c & 0 & 0 & K_{s3}^c \\ -K_{s1}^c & 0 & 0 & K_{s2}^c & K_{s1}^c \\ 0 & -K_{s1}^c & K_{s2}^c & 0 & 0 & K_{s1}^c \\ 0 & -K_{s2}^c & K_{s4}^c & 0 & 0 & K_{s2}^c & K_{s3}^c \\ -K_{s2}^c & 0 & 0 & K_{s4}^c & K_{s2}^c & 0 & 0 & K_{s3}^c \end{bmatrix} \quad K_{s1}^c = 12$$

speed amplitude can be utilized to detect the crack.
(3) Based on the RBF network and PRNN, the quantitative crack fault diagnosis method is proposed. In the case where both the crack depth and position are uncertain, Adopting the analyzed dynamic characteristics as input, the maximum percentage error between the trained RBF network's output results and the ground truth is 7.56%. Besides, the approximate recognition accuracy of the crack position obtained by the PRNN can reach 98.2%. The requirements of crack fault diagnosis are satisfied preliminarily.

$$K_{s2}^c = 6l$$

$$K_{s3}^c = (4+2\varphi_s+\varphi_s^2)l^2$$

$$K_{s4}^c = (2-2\varphi_s-\varphi_s^2)l^2$$

$$\xi = \frac{z}{l}, \varphi_s = \frac{12EI}{\mu AGl^2}$$

Jin et al. Chinese Journal of Mechanical Engineering   (2023) 36:35

Page 16 of 18

$$\boldsymbol{K}_{\mathrm{s}}^{\mathrm{s}} = \frac{EI\varphi_s}{(1+\varphi_s^2)l^3}\begin{bmatrix} K_{s1}^s & & & & & & & \text{sym.} \\ 0 & K_{s1}^s & & & & & & \\ 0 & -K_{s2}^s & K_{s3}^s & & & & & \\ -K_{s2}^s & 0 & 0 & K_{s3}^s & & & & \\ -K_{s1}^s & 0 & 0 & K_{s2}^s & K_{s1}^s & & & \\ 0 & -K_{s1}^s & K_{s2}^s & 0 & 0 & K_{s1}^s & & \\ 0 & -K_{s2}^s & K_{s3}^s & 0 & 0 & K_{s2}^s & K_{s3}^s & \\ -K_{s2}^s & 0 & 0 & K_{s3}^s & K_{s2}^s & 0 & 0 & K_{s3}^s \end{bmatrix}$$

$K_{s1}^s = 12 K_{s2}^s = 6l, K_{s3}^s = (2-\varphi_s)l^2, K_{s4}^s = (4+\varphi_s)l^2$

$J_{s1} = 36$

$$\boldsymbol{M}_{\mathrm{s}}^{\mathrm{c}} = \frac{\rho_s l}{(1+\varphi_s^2)}\begin{bmatrix} M_{s1}^c & & & & & & & \text{sym.} \\ 0 & M_{s1}^c & & & & & & \\ 0 & -M_{s4}^c & M_{s2}^c & & & & & \\ -M_{s4}^c & 0 & 0 & M_{s2}^c & & & & \\ M_{s3}^c & 0 & 0 & -M_{s5}^c & M_{s1}^c & & & \\ 0 & M_{s3}^c & -M_{s5}^c & 0 & 0 & M_{s1}^c & & \\ 0 & M_{s5}^c & -M_{s6}^c & 0 & 0 & M_{s4}^c & M_{s2}^c & \\ M_{s5}^c & 0 & 0 & -M_{s6}^c & M_{s4}^c & 0 & 0 & M_{s2}^c \end{bmatrix}$$

$M_{s1}^c = 13/35 + 7/10\varphi_s + \varphi_s^2$

$M_{s2}^c = (1/105 + 1/60\varphi_s + 1/120\varphi_s^2)l^2$
$M_{s3}^c = 9/70 + 3/10\varphi_s + 1/6\varphi_s^2$
$M_{s4}^c = (11/210 + 11/120\varphi_s + 1/24\varphi_s^2)l$
$M_{s5}^c = (13/420 + 3/40\varphi_s + 1/24\varphi_s^2)l,$

$M_{s6}^c = (1/140 + 1/60\varphi_s + 1/120\varphi_s^2)l^2$

$J_{s2} = 3l - 15l\varphi_s$

$J_{s3} = l^2 + 5l^2\varphi_s - 15l^2\varphi_s^2$

$J_{s4} = 4l^2 + 5l^2\varphi_s + 10l^2\varphi_s^2$

$$\boldsymbol{M}_{\mathrm{s}}^{\mathrm{s}} = \frac{j_d}{(1+\varphi_s^2)l}\begin{bmatrix} M_{s1}^s & & & & & & & \text{sym.} \\ 0 & M_{s1}^s & & & & & & \\ 0 & -M_{s4}^s & M_{s2}^s & & & & & \\ -M_{s4}^s & 0 & 0 & M_{s2}^s & & & & \\ -M_{s1}^s & 0 & 0 & -M_{s4}^s & M_{s1}^s & & & \\ 0 & -M_{s1}^s & M_{s4}^s & 0 & 0 & M_{s1}^s & & \\ 0 & -M_{s4}^s & M_{s3}^s & 0 & 0 & -M_{s4}^s & M_{s2}^s & \\ -M_{s4}^s & 0 & 0 & M_{s3}^s & -M_{s4}^s & 0 & 0 & M_{s2}^s \end{bmatrix}$$

$M_{s1}^s = 6/5, M_{s2}^s = (2/15 + 1/6\varphi + 1/3\varphi^2)l^2,$
$M_{s3}^s = (-1/30 - 1/6\varphi + 1/6\varphi^2)l^2, M_{s4}^s = (1/10 - 1/2\varphi)l$

$$\boldsymbol{J}_{\mathrm{s}} = \frac{j_p}{30(1+\varphi_s^2)l}\begin{bmatrix} 0 & & & & & & & \text{antisym.} \\ J_{s1} & 0 & & & & & & \\ -J_{s2} & 0 & 0 & & & & & \\ 0 & -J_{s2} & J_{s4} & 0 & & & & \\ 0 & J_{s1} & -J_{s2} & 0 & 0 & & & \\ -J_{s1} & 0 & 0 & -J_{s2} & J_{s1} & 0 & & \\ -J_{s2} & 0 & 0 & J_{s3} & J_{s2} & 0 & 0 & \\ 0 & -J_{s1} & -J_{s3} & 0 & 0 & J_{s2} & J_{s4} & 0 \end{bmatrix}$$

Authors' Information
Yuhong Jin, born in 1998, is currently a PhD candidate at *School of Astronautics, Harbin Institute of Technology, China*, in 2022. His research interests include machine learning, intelligent fault diagnosis and nonlinear dynamics.
Lei Hou, born in 1987, is currently an associate professor and a PhD candidate supervisor at *School of Astronautics, Harbin Institute of Technology, China*. He received his PhD degree from *Harbin Institute of Technology, China*, in 2015. His main research interests include nonlinear dynamics, rotor dynamics, vibration control, fault diagnosis.
Zhenyong Lu, born in 1988, is currently a lecturer at *Institute of Dynamics and Control Science, Shandong Normal University, China*. He received his PhD degree from *Harbin Institute of Technology, China*, in 2017. His research interests include nonlinear dynamics, rotor dynamics, crack fault diagnosis.
Yushu Chen, born in 1931, is currently a professor and a PhD candidate supervisor at *School of Astronautics, Harbin Institute of Technology, China*. His main research interests include nonlinear dynamics and its applications in engineering.

Competing interests
The authors declare no competing financial interests.

References

[1] B X Tchomeni, A Alugongo. Modelling and dynamic analysis of an unbalanced and cracked cardan shaft for vehicle propeller shaft systems. *Appiled Sciences*, 2021, 11(17): 8132.

[2] I W Mayes, W G R Davies. Analysis of the response of a multi-rotor-bearing system containing a transverse crack in a rotor. *Journal of Vibration and Acoustics*, 1984, 106(1): 139–145.

[3] M A Al-Shudeifat, E A Butcher. New breathing functions for the transverse breathing crack of the cracked rotor system: approach for critical and subcritical harmonic analysis. *Journal of Sound and Vibration*, 2011, 330(3): 526–544.

[4] A K Darpe, K Gupta, A Chawla. Dynamics of a two-crack rotor. *Journal of Sound and Vibration*, 2003, 259(3): 649–675.

[5] L Xiang, X Y Gao, A J Hu. Nonlinear dynamics of an asymmetric rotor-bearing system with coupling faults of crack and rub-impact under oil-film forces. *Nonlinear Dynamics*, 2016, 86(2): 1057–1067.

[6] L Hou, Y S Chen. Super-harmonic responses analysis for a cracked rotor system considering inertial excitation. *Science China Technological Sciences*, 2015, 58(11): 1924–1934.

[7] Z Y Lu, L Hou, Y S Chen, et al. Nonlinear response analysis for a dual-rotor system with a breathing transverse crack in the hollow shaft. *Nonlinear Dynamics*, 2016, 83(1–2): 169–185.

[8] C Fu, Y D Xu, Y F Yang, et al. Dynamics analysis of a hollow-shaft rotor system with an open crack under model uncertainties. *Communications in Nonlinear Science and Numerical Simulation*, 2020, 83: 105102.

[9] S Wang, C X Bi, J Z Li, et al. Parametric instability of anisotropic rotor-bearing systems with a transverse crack. *Journal of Sound and Vibration*, 2019, 443: 253–269.

[10] Y Liu, Y L Zhao, Z Q Lang, et al. Weighted contribution rate of nonlinear output frequency response functions and its application to rotor system fault diagnosis. *Journal of Sound and Vibration*, 2019, 460: 114882.

[11] N Kushwaha, V N Patel. Nonlinear dynamic analysis of two-disk rotor system containing an unbalance influenced transverse crack. *Nonlinear Dynamics*, 2022, https://doi.org/10.1007/s11071-022-07893-7.

[12] M Yang, H Xuan, W Xiong, et al. Analytical bending stiffness model of composite shaft with breathing fatigue crack. *Mechanics of Advanced Materials and Structures*, 2022, https://doi.org/10.1080/15376494.2022.2092794.

[13] K Ganguly, H Roy. A novel geometric model of breathing crack and its influence on rotor dynamics. *Journal of Vibration and Control*, 2022, 28(21–22): 3411–3425.

[14] D H Zhang, Y H Zhao, Z D Wang, et al. Review on diagnosis techniques for intermittent faults in dynamic systems. *IEEE Transactions on Industrial Electronics*, 2020, 67(3): 2337–2347.

[15] L Yang, H X Chen. Fault diagnosis of gearbox based on RBF-PF and particle swarm optimization wavelet neural network. *Neural Computing and Applications*, 2019, 31: 4463–4478.

[16] T Han, L W Zhang, Z J Yin, et al. Rolling bearing fault diagnosis with combined convolutional neural networks and support vector machine. *Measurement*, 2021, 177: 109022.

[17] B Munoz-Abella, A Ruiz-Fuentes, P Rubio, et al. Cracked rotor diagnosis by means of frequency spectrum and artificial neural networks. *Smart Structures and Systems*, 2020, 25(4): 459–469.

[18] C Z Guo, J Yan, W Yang. Crack detection for a Jeffcott rotor with a transverse crack: An experimental investigation. *Mechanical Systems and Signal Processing*, 2017, 83: 260–271.

[19] R K Vashisht, Q Peng. Crack detection in the rotor ball bearing system using switching control strategy and short time Fourier Transform. *Journal of Sound and Vibration*, 2018, 432: 502–529.

[20] X A Yan, M P Jia. A novel optimized SVM classification algorithm with multi-domain feature and its application to fault diagnosis of rolling bearing. *Neurocomputing*, 2018, 313: 47–64.

[21] G F Bin, J J Gao, X J Li, et al. Early fault diagnosis of rotating machinery based on wavelet packets-Empirical mode decomposition feature extraction and neural network. *Mechanical Systems and Signal Processing*, 2012, 27: 696–711.

[22] S Ma, F L Chu. Ensemble deep learning-based fault diagnosis of rotor bearing systems. *Computers in Industry*, 2019, 105: 143–152.

[23] D Y Wang, C R Hua, D W Dong, et al. Crack parameters identification based on a kriging surrogate model for operating rotors. *Shock and Vibration*, 2018: https://doi.org/10.1155/2018/9274526.

[24] L M Wang, Y M Shao. Crack fault classification for planetary gearbox based on feature selection technique and K-means clustering method. *Chinese Journal of Mechanical Engineering*, 2018, 31(4): https://doi.org/10.1186/s10033-018-0202-0.

[25] B Li, X F Chen, Z J He. Three-steps-meshing based multiple crack identification for structures and its experimental studies. *Chinese Journal of Mechanical Engineering*, 2013, 26: 400–405.

[26] M A Al-Shudeifat. Impact of non-synchronous whirl on post-resonance backward whirl in vertical cracked rotors. *Journal of Sound and Vibration*, 2022, 520: 116605.

[27] J S Xie, W Cheng, Y Y Zi. Modified breathing mechanism model and phase waterfall plot diagnostic method for cracked rotors. *Journal of Mechanical Science and Technology*, 2018, 32: 2827–2539.

[28] Z N Li, Y L Li, D Wang, et al. Dynamic characteristics of rotor system with a slant crack based on fractional damping. *Chinese Journal of Mechanical Engineering*, 2021, 34: 27.

[29] H M Mobarak, H L Wu, C H Yang. Location dependence of breathing mechanism for a slant crack in a shaft. *Fatigue & Fracture of Engineering Materials & Structures*, 2020, 43(11): 2515–2526.

[30] Y H Wang, X Xiong, X Hu. Vibration and stability analysis of a bearing–rotor system with transverse breathing crack and initial bending. *Machines*, 2021, 9(4): 79.

[31] J Spagnol, H L Wu, C H Yang. Application of non-symmetric bending principles on modelling fatigue crack behaviour and vibration of a cracked rotor. *Applied Sciences*, 2020, 10(2): 717.